










Local structural investigation across the magnetic transition in the type-II multiferroic material FeVO₄

Ganesh Bera ^{1,2}, Akash Surampalli ^{3,1}, Maximiliano L. Riddick ⁴, V. Raghavendra Reddy ^{1,*}, V. G. Sathe ¹,
G. R. Turpu ², Edmund Welter ⁵, Archana Sagdeo ^{6,7} and Carlo Meneghini ^{8,†}

¹UGC-DAE CSR, University Campus, Khandwa Road, Indore 452001, India

²Department of Pure and Applied Physics, Guru Ghasidas Vishwavidyalaya, Bilaspur 495009, India

³Department of Materials Engineering, Indian Institute of Science, Bangalore-560012, India


⁴CMaLP (Centro de Matemática de La Plata), Facultad de Ciencias Exactas, Universidad Nacional de La Plata, Buenos Aires-1900, Argentina

⁵Deutsches Elektronen-Synchrotron—A Research Centre of the Helmholtz Association, Hamburg 22607, Germany

⁶Synchrotron Utilization Section, RRCAT, Indore 452017, India

⁷Homi Bhabha National Institute, Training School Complex, Anushakti Nagar, Mumbai 400094, India

⁸Dipartimento di Scienze, Università di Roma Tre, I-00146 Roma, Italy

 (Received 16 July 2023; revised 14 December 2023; accepted 23 January 2024; published 20 February 2024)

The structural modifications associated with magnetic and multiferroic transitions in FeVO₄ polycrystalline samples have been investigated using complementary techniques, including synchrotron radiation x-ray diffraction (XRD), Raman spectroscopy, and x-ray absorption fine-structure spectroscopy (XAFS). Temperature-dependent measurements reveal unveiled details of the local structural modifications intimately related to the spin-lattice coupling. This study is particularly focused on illuminating the changes occurring crossing the two distinct antiferromagnetic transition temperatures at 21.8 (±0.5) K (T_{N1}) and 15.6 (±0.5) K (T_{N2}) in the FeVO₄. The combined analysis of XRD, Raman, and XAFS spectra rules out major modification of the Fe valence state or the average Fe-O_n coordination geometry related to the transitions at T_{N1} and T_{N2} . On the contrary, structural modifications are revealed in the Fe-Fe, Fe-V, and Fe-O-V path distances as a function of temperature, attributable to changes in the tilting and rotation of Fe-O_n and/or V-O_n polyhedra, likely representing the microstructural fingerprint of changes in the super-super-exchange interactions along the Fe³⁺-O-V⁵⁺-O-Fe³⁺ pathway.

DOI: [10.1103/PhysRevB.109.075138](https://doi.org/10.1103/PhysRevB.109.075138)

I. INTRODUCTION

The study of multiferroic/magnetoelectric materials has been of great interest in recent years due to their multifunctional properties and their technological importance for device and spintronic applications [1–4]. FeVO₄ is among the interesting and unique type-II multiferroic materials. It has triclinic (P-1) crystal symmetry and is made by three inequivalent Fe sites—two distorted FeO₆ octahedral and one distorted FeO₅ trigonal bipyramid site—connected by VO₄ tetrahedral groups [5]. FeVO₄ exhibits large spin-charge-lattice coupling displaying multiferroicity driven by spiral magnetic ordering at low temperatures [6]. Lately, there has been some research interest in pure and doped FeVO₄ compounds as potential *n*-type multimetal oxide semiconductors because they exhibit structural phase transitions that are dependent on external pressure [7,8]. FeVO₄ exhibits two successive antiferromagnetic (AFM) transitions on cooling, one at $T_{N1} = 21.8(\pm 0.5)$ K providing a collinear incommensurate magnetic structure, and a second at $T_{N2} = 15.6(\pm 0.5)$ K characterized

by noncollinear incommensurate or magnetic spiral structure as reported in the literature [9]. Because of the geometric arrangement of Fe ions in the lattice, FeVO₄ also has a strongly frustrated magnetic nature. An improper ferroelectric ordering with finite spontaneous electrical polarization at the temperature $T_{N2} \simeq 16$ K also gets developed simultaneously with the spiral incommensurate magnetic phase [10]. In FeVO₄, the magnetic direct exchange or superexchange (SE) paths are not present. Such a feature can be attributed to the large interatomic distances between neighboring magnetic ions (Fe), which exceed 3.0 Å. These long distances provide negligibly small direct overlap exchange integrals, preventing a strong enough coupling to sustain long-range magnetic order. Additionally, due to edge-shearing FeO_n polyhedra, the 180° SE path between nearest magnetic ions (Fe) via Fe-O-Fe links is lacking. Instead, the magnetic modulation is primarily determined by a network of super-super-exchange (SSE) interactions through the Fe³⁺-O-V⁵⁺-O-Fe³⁺ pathway. These pathways are formed by S-shaped magnetic loops (clusters) that connect an odd number of Fe³⁺ crystallographic sites [Fe(1), Fe(2), and Fe(3)] of edge-sharing FeO_n (*n* = 5, 6) polyhedra repeated twice in reverse order: Fe(1)-Fe(2)-Fe(3)-Fe(3)-Fe(2)-Fe(1), linked by VO₄ tetrahedral groups [10]. This arrangement leads to geometrical frustration as well as

* varimalla@yahoo.com; vrreddy@csr.res.in

† carlo.meneghini@uniroma3.it

magnetic frustration in the system, which plays a crucial role in promoting noncollinearity and inducing ferroelectricity. At the second transition (T_{N2}), a spiral spin modulation occurs, resulting in varying amplitudes of magnetic moment at different Fe sites. This spiral spin modulation, caused by magnetic frustration with dominating SSE interactions, is correlated with moment reductions or spin rotations in the incommensurate magnetic phases [10]. As a result, there is a possibility of the presence of different charge valencies for Fe at different inequivalent Fe sites, which may vary across the phase transitions. Determining the direction of polarization solely from the magnetic structure is challenging due to the low symmetry of the crystal structure of FeVO_4 , with distorted inequivalent crystal sites of magnetic ions. The direction of polarization also depends on the details of microscopic magnetoelectric interactions, which are influenced by interatomic bond distances and the dominating SSE interaction path at low temperatures [10–15].

Because of such complexity, it is important to reveal the local crystal structure (in atomic scale) and electronic state of the magnetic sites in FeVO_4 , as well as how they evolve across the magnetic transitions, to understand the role of the exchange interaction paths and the onset of ferroelectric ordering.

With these considerations in mind, this paper presents a detailed investigation on FeVO_4 aimed at revealing atomic-scale structural modification associated with the magnetic transitions, using temperature-dependent synchrotron radiation x-ray diffraction (SR-XRD), Raman spectroscopy, and x-ray absorption fine structure (XAFS) spectroscopy.

II. EXPERIMENTAL METHODS

A polycrystalline FeVO_4 compound was synthesized by the standard solid-state reaction method. The synthesis and room-temperature structural analysis details were described in one of our previous reports [16]. The temperature-dependent SR-XRD measurements on FeVO_4 powders were carried out in the 5–300 K temperature range at the x-ray diffraction beamline (BL-12), Indus-2, RRCAT, Indore [17] using an angle-dispersed setup based on a MAR-345 Area detector. A uniform amount of finely ground FeVO_4 powder was deposited on Kapton tape and mounted on the liquid He flow-type cryostat on the Image plate sample holder setup. The diffraction geometry (sample to detector distance, $d = 200$ mm, and detector perpendicularity to the x-ray beam) was calibrated refining the diffractograms of a reference (LaB_6) sample. The 2D diffractograms were integrated using the FIT2D [18] software to obtain standard intensity versus 2θ 1D diffractograms. Integration of full Debye rings from 2D diffractograms ensures the highest signal-to-noise ratio, particularly suitable for revealing parasitic phases, and significantly reduces the effects of privileged orientations, making the data particularly suitable for structure refinement. Crystallographic structural parameters as a function of temperature were obtained by refining the 1D patterns via the full profile Rietveld method using the FULLPROF software [19]. The crystal structures were visualized using the VESTA software [20], which also allows for calculating the geometrical parameters (interatomic distances and bond angles).

Temperature-dependent Raman and XAFS spectroscopy data were used to extract information about the local atomic structure behavior as a function of temperature across the magnetic transitions. The Raman spectra were measured in the 5–300 K range using a liquid He-based flow-type cryostat and a He-Ne laser ($\lambda = 632.8$ nm) as the excitation source coupled with a Jobin Yvon Horibra LABRAM spectrometer.

The x-ray absorption spectroscopy (XAS) experiments were carried out at the P65 beamline of PETRA-III synchrotron radiation storage ring DESY (Hamburg, Germany) [21] in distinct experiments for Fe and V K -edge measurements. The FeVO_4 sample was manually ground to a fine powder, mixed with BN matrix, and pressed into a uniform pellet suitable for handling. The sample was positioned within a helium cryostat and cooled to 5 K (10 K) for conducting vanadium (iron) K -edge experiments and allowed to stabilize 15 min before measurements. The XAS spectra were collected in transmission geometry at V ($E_{V^o} = 5465$ eV) and Fe ($E_{\text{Fe}^o} = 7112$ eV) K edges, at selected temperatures in the 5–75 K (V) and 10–50 K (Fe) temperature range. Waiting 15 min stabilization time for each temperature step, 2.5 K temperature steps were used close to the magnetic transition, in between 10 and 25 K, and 5/10 K far from it.

The XAS spectra were measured running the beamline in quick scan mode (Q-XAS). Up to three scans were acquired for each temperature point collecting about 8×10^3 energy points each, in the 5300–6470 and 6970–8120 eV energy ranges for V and Fe K -edge experiments, respectively. The Q-XAS scans were rebinned using a Python script based on Numpy library [22] (code available on request). The script divided the energy scale into large preedge steps ($\Delta E = 5$ eV), thin energy steps ($\Delta E = 0.3$ eV) across the V/Fe absorption edges ($E_o - 10$ eV to $E_o + 20$ eV), and fixed $\Delta k = 0.02 \text{ \AA}^{-1}$ in the extended region; the experimental data in each interval were averaged. The rebinned spectra of each scan were checked for accurate energy scale alignment and averaged to improve data statistics at each temperature step. Statistical noise was assessed by calculating the average standard deviation of the normalized XAS signal with respect to a high degree polynomial spline through the data [23] resulting in better than $\sigma_{\text{stat}} \simeq 1.5 \times 10^{-4}$.

III. DATA ANALYSIS

A. SR-XRD

The temperature-dependent SR-XRD pattern in the temperature range 5–50 K and at 300 K and the Rietveld refinement of the room-temperature (RT) SR-XRD pattern of the FeVO_4 compound are shown in the supplemental material (SM), Figs. S1(a,b) [24], respectively. The Rietveld refinement of other temperature-dependent SR-XRD patterns is illustrated in Fig. S2 (see the SM [24]) along with the refinements parameters. Variations of lattice parameters and unit-cell volume across the magnetic transitions in FeVO_4 were reported in our previous study [9]; the crystallographic changes associated with the transitions demonstrated the presence of strong magnetolattice coupling in the system. Furthermore, the high signal-to-noise ratio of the 2D SR-XRD data free of the preferred orientation permits reliable refinement of oxygen positions in the unit cell, allowing tracking of

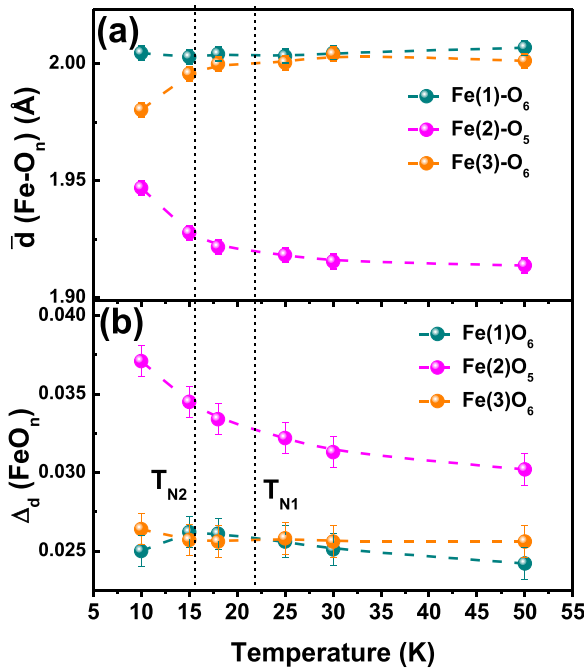


FIG. 1. Changes in the average Fe-O bond distances (\bar{d}) (a) and the distortion parameter (Δ_d) (b) of Fe-O_n polyhedra ($n = 5, 6$) concerning temperature corresponding to three different crystal sites of Fe in FeVO₄. Symbols are the experimental data points with error bars, while dashed lines are guides to the eyes.

the modifications of crystallographic Fe-O_n polyhedra across magnetic transitions, in particular average Fe-O distances d_i within the polyhedra, and the FeO_n polyhedra distortion Δ_d defined as

$$\Delta_d = \frac{1}{n} \sqrt{\sum_{i=1}^n \left[\frac{d_i - \bar{d}}{\bar{d}} \right]^2}, \quad (1)$$

where n is the coordination number, and \bar{d} is the average Fe-O site distances for a specific polyhedron.

The results of XRD Rietveld data refinement as a function of temperature demonstrate that FeVO₄ maintains its triclinic symmetry in the whole temperature range, until 5 K. We have shown that the lattice parameters depict the major changes crossing T_{N2} [9] while the effect at T_{N1} is definitively weaker. The crystallographic structures obtained from the Rietveld refinements have been visualized using VESTA software [refer to Fig. S3(a) of the SM [24]]. The geometrical parameters of the FeO_n crystallographic polyhedra have been evaluated at different temperatures. The intersite distances and distortion parameters for the three Fe sites are summarized in Table SI (see the SM [24]). Additionally, the average Fe-O intersite distance and polyhedron distortion parameter (Δ_d) have been plotted in Fig. 1, illustrating their variation with temperature.

The crystallographic structure of FeVO₄ belongs to the P-1 space group and is characterized by three inequivalent Fe³⁺ crystallographic sites yielding two FeO₆ octahedra [Fe(1), Fe(3)] and one FeO₅ trigonal bipyramid [Fe(2)]. The fundamental magnetic unit comprises S-shaped clusters formed

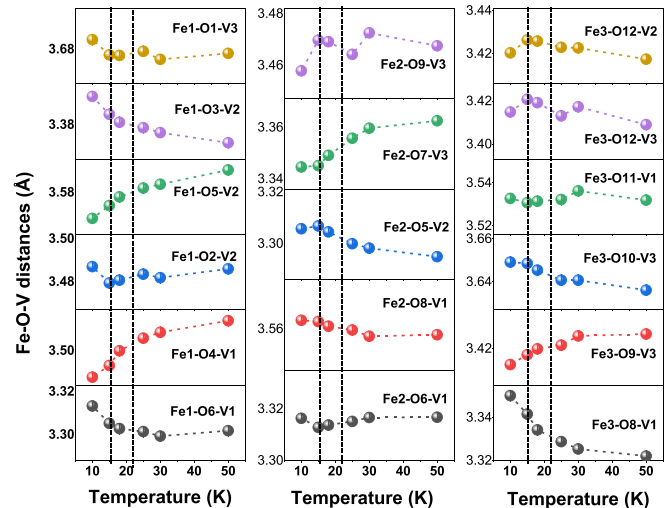


FIG. 2. The variation of the Fe-V (direct) crystallographic distances as a function of temperature corresponds to three different inequivalent crystal sites of Fe and V in the unit cell of FeVO₄ suggesting the possible changes in Fe-O-V angles as presented in the present figure. All the plots are shown using the same vertical scale. Symbols are the experimental data points with error bars, while dashed lines are guided to the eyes.

by six alternating edge-sharing FeO_n units Fe(1)-Fe(2)-Fe(3)-F(3)-Fe(2)-Fe(1) [refer to Fig. S3(b) of the SM [24], and Ref. [10]] providing intracluster Fe-Fe (exchange) and Fe-O-Fe (super-exchange) interactions which does not exist here. The corner-shared VO₄ tetrahedral units provide interchain connections leading to the emergence of effective Fe-O-V-O-Fe super-super-exchange (SSE) intercluster interactions. The FeO_n and VO₄ polyhedra are irregular, leading to different Fe/V-O distances and Fe-O-Fe/V angles whose evolution with temperature across $T_{N1,2}$ would provide insights into the coupling mechanisms in the magnetic phases.

Figures S3(c,d) of the SM [24] show different V neighbors around the three distinct Fe ions and one of the possible orientations of the Fe atom surrounded by six VO₄ tetrahedral groups, respectively. Additionally, the study focuses on the temperature variation of FeO_n and VO₄ tilting polyhedra, considering the Fe-Fe and Fe-V distances connected through oxygen atoms, which may result in changes in the Fe-O-Fe and Fe-O-V angles, respectively. Figure S3(e) of the SM [24] presents three different intracluster Fe-Fe distances as a function of temperature. In addition to the aforementioned analysis, the study also includes an investigation of the changes in Fe-O-V angles with temperature. To accomplish this, the Fe-V (direct) distances, which are mediated through oxygen atoms, have been calculated for the three distinct FeO_n polyhedra surrounded by different VO₄ tetrahedral groups. These Fe-V distances are tabulated in Table SII (see the SM [24]). Figure 2 illustrates the different Fe-V distances corresponding to the two FeO₆ octahedra and one FeO₅ trigonal bipyramid connected to VO₄ tetrahedra as a function of temperature as demonstrated in the figure. The variation of Fe-O-V bond angles with temperature is presented in Fig. S4 (see the SM [24]).

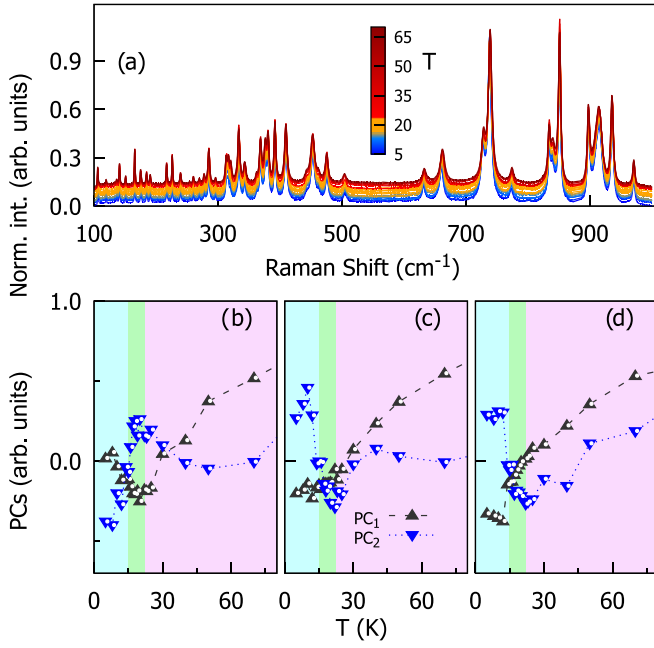


FIG. 3. Top panel (a): Temperature-dependent normalized Raman spectra of FeVO_4 measured in the 5–100 K temperature range. Bottom panels: the first two principal component weights ($w_{1,2}$) as a function of temperature calculated at 100–300 cm^{-1} (b), 300–520 cm^{-1} (c), and 600–1000 cm^{-1} (d), depict evident changes crossing the T_{N1} and T_{N2} temperatures.

B. Raman spectroscopy

Raman spectroscopy provides information about the strength of atomic interactions by directly investigating the atomic vibrations of molecules. The Raman spectroscopic studies of FeVO_4 as a function of temperature provide insights into the relationship between the evolution of magnetic order and changes in atomic lattice dynamics. First, the principal component analysis (PCA) method [25] is used to identify global changes in Raman spectra caused by magnetic transitions. PCA serves as a multivariate statistical method that, when applied to a data set, identifies the components responsible for the variance within the data set. These components are the eigenvectors of the covariance matrix, ranked in order of significance based on their corresponding eigenvalues. Each original spectrum in the data set can be reproduced as a linear combination (LC) of fundamental eigenvectors (PC) $\sum_i w_i \text{PC}_i$ with their coefficients w_i being the relative contribution of each component. The first components in the LC likely represent real differences between the data, while the subsequent components become progressively dominated by uncertainty and statistical noise. Looking at the evolution of the weight w_i of these first components offers a convenient way to discern even tiny changes coming from real effects, and drive the quantitative analysis. The raw Raman spectra were imported into Orange software [26], the background was subtracted using the rubber band method [27], and the spectra were normalized by the standard normal variation method. Finally, the PCA was carried out in selected Raman shift regions, and the weights of the first two components are reported as a function of temperature (Fig. 3). The temperature

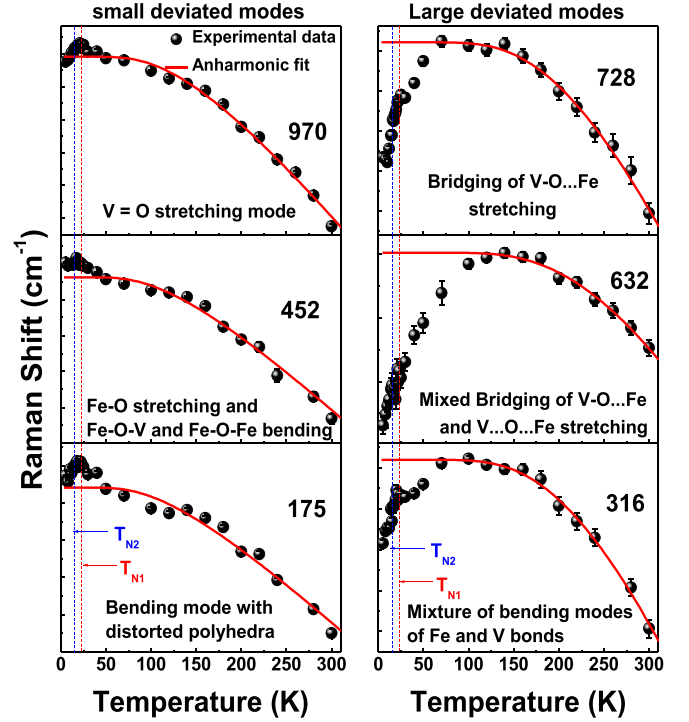


FIG. 4. Anharmonic model fitting of the profile of the temperature dependence of Raman shifts (cm^{-1}) for selected modes of vibrations as presented in the figure ranging from 200 to 1000 cm^{-1} in the temperature range 5–300 K (symbols are the experimental data points, and the solid red line is fit with the anharmonic model fit as described in the text). The vertical dashed lines represent the transition temperatures T_{N1} (red) and T_{N2} (blue).

dependence of the first $w_{1,2}$ shows substantial changes heating the samples across the transition temperatures, demonstrating that the magnetic transitions have direct effects on the vibrational properties, and then on the strength of the atomic interactions. To obtain quantitative details about these changes, we proceed with the fitting of the experimental spectra.

All the temperature-dependent Raman spectra were fitted with Lorentz shape divided into three regions [region-I, region-II, and region-III as shown in Fig. S5 (see the SM [24])] for better fitting of such a large number of Raman modes (> 45 modes) present in the spectra. The behavior of anharmonic phonons with temperature, which is caused by the anharmonic phonon-phonon interactions in a system, can provide valuable insights into the underlying physics. So, the obtained Raman shift as a function of the temperature of selected modes was fitted with the anharmonic model

$$\omega(T) = \omega_0 + C \left[1 + \frac{2}{e^x - 1} \right],$$

where $x = \hbar\omega_0/2k_B T$; ω_0 is the Raman frequency at 0 K, and C is a fitting parameter [28] as shown in Fig. 4. From the anharmonic model analysis, it is observed that the Raman shifts correspond to the bridging of V-O...Fe stretching and mixed bridging of V-O...Fe and V...O...Fe stretching modes (around 728 and 632 cm^{-1} ; see the right panel of Fig. 4), and the mixture of bending modes, involving bonds

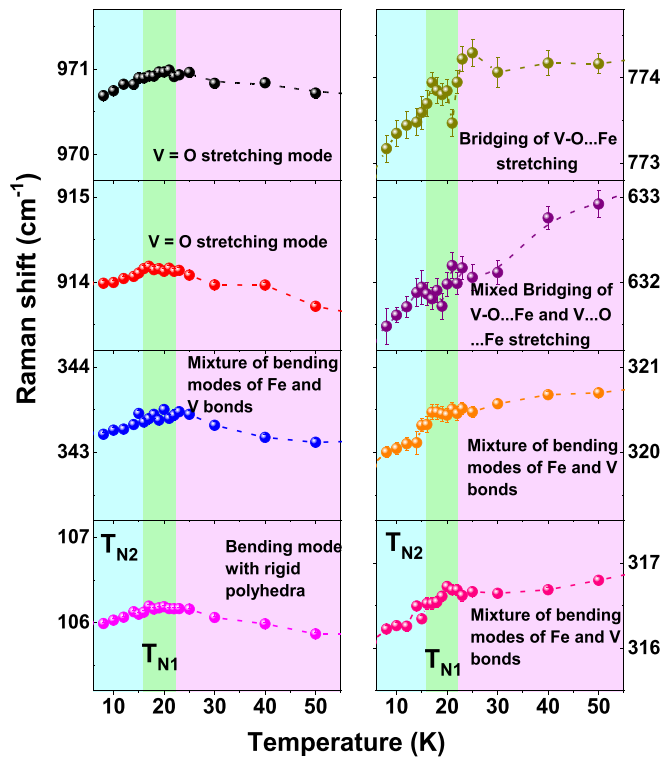


FIG. 5. Temperature variation of selected Raman modes corresponding to (left panel) the $V = O$ stretching modes (970 and 914 cm^{-1}), the mixture of bending modes of Fe and V bonds (343 cm^{-1}), and bending modes with rigid polyhedra (106 cm^{-1}), showing anomalies across the T_{N1} transitions; (right panel) bridging of $V-O \cdots Fe$ stretching (774 cm^{-1}), mixed bridging of $V-O \cdots Fe$ and $V \cdots O \cdots Fe$ stretching (632 cm^{-1}), and the mixture of bending modes of Fe and V bonds (320 and 316 cm^{-1}) shows anomalies across both T_{N1} and T_{N2} transitions as illustrated in the figure. The Raman shift scale is applied to all the panels for the sake of comparison.

of both Fe and V (around 316 cm^{-1}) as a function of temperature, drastically deviates from the anharmonic behavior on cooling below roughly 70 K, being quite far with respect to the multiferroic transitions. On the other hand, the other Raman modes corresponding to the $V-O$ stretching (around 970 cm^{-1}), bending modes together with $Fe-O$ stretching (around 452 cm^{-1}), a mixture of bending modes involving both Fe and V along with all the distorted polyhedra (175 cm^{-1}), and bending modes with rigid polyhedra (below 170 cm^{-1}) [29] show only a small deviation from the anharmonic behavior, as can be seen in the left panel of Fig. 4. The other anharmonic model fitting of the remaining representative modes corresponding to these modes of vibration as mentioned above is shown in Fig. S6 (see the SM [24]). The low-temperature behavior across the transitions of some of these modes is illustrated in Fig. 5, as discussed in detail in the next section.

C. XAFS spectroscopy

V and Fe K -edge XAS spectra were treated along the standard procedures for preedge removal, postedge atomic background subtraction (α_o), and edge discontinuity (jump)

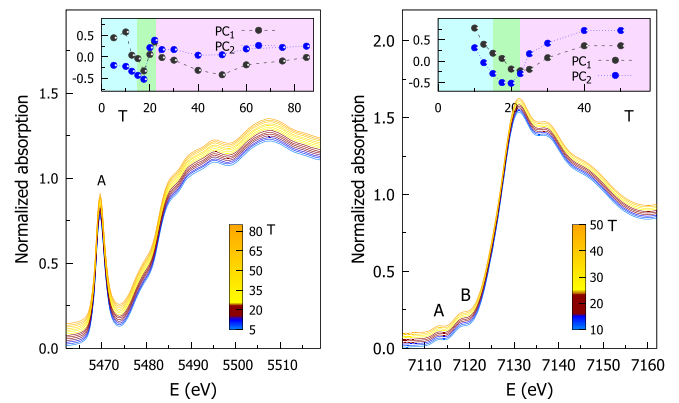


FIG. 6. Normalized V (left panel) and Fe (right panel) K -edge XANES spectra measured on $FeVO_4$ as a function of temperature across the magnetic transitions, slightly vertically shifted for clarity. The top insets demonstrate the evolution of the first two principal component weights as a function of temperature. The $w_{1,2}$ have been normalized to their respective ranges for the sake of comparison.

normalization [23,30]. The edge energy (E_o) defining the origin of the photoelectron wave vector $k = \hbar^{-1} \sqrt{2m_e(E - E_o)}$ (m_e being the electron mass) has been selected at the half of the edge raising, and refined during the analysis (see below for details). The XAS spectra were uniformly processed using identical sets of parameters to normalize the XAFS signal and to refine the spectra. This approach increases the sensitivity to detect even weak structural changes that could result from temperature variations across the magnetic transition.

Figure 6 illustrates the V and Fe near-edge (XANES) normalized spectra, measured as a function of temperature demonstrating the very equal shape across the magnetic transition temperatures. The V XANES features are consistent with the V^{5+} valence state [31], the intense preedge peak being consistent with VO_4 tetrahedral units. The Fe XANES position is consistent with the Fe^{3+} valence state [32,33]. PCA makes it possible to highlight, on a statistical basis, even small differences between the data that would otherwise be difficult to detect using a profile fit analysis. The weights of the first two components, $w_{1,2}$, are shown as a function of temperature in the insets of Fig. 6. In both cases, the $w_{1,2}$ of the show changes in the temperature-dependent trend that correlates with the magnetic transitions, although smoother for Fe and sharper for V. The XANES features have been quantitatively analyzed by fitting the experimental data to a curve made up of an arco-tangent curve reproducing the rise of the main edge, and one/two Lorentzian (V/Fe edges) peaks reproducing the preedge features A/A-B.

Figure 7 presents the k -weighted extended x-ray absorption fine structure (EXAFS) signals $k\chi(k)$, measured at the V and Fe K edges. The color scheme highlights the magnetic transition temperatures. The Fourier transforms are presented in Fig. S7 (see the SM [24]) for completeness. As for the XANES region, also in the EXAFS region, the changes as a function of temperature are weak and indistinguishable to a qualitative inspection. Nevertheless, the PCA (not shown) reveals specific changes in the trend of w_1 and w_2 crossing the magnetic transition temperatures, and the EXAFS data

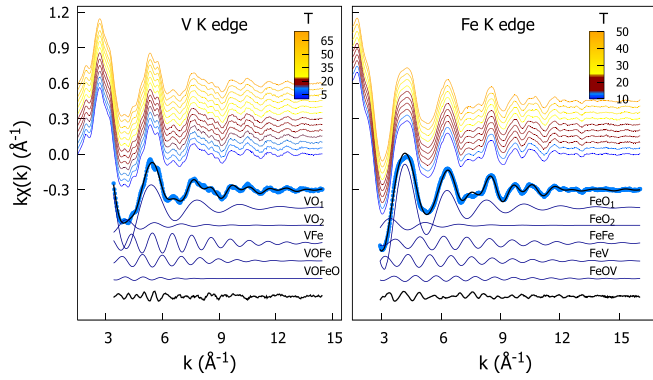


FIG. 7. Top curves (vertically shifted for sake of clarity) represent the k -weighted experimental EXAFS spectra measured as a function of temperature at the V (left panel) and Fe (right panel) K edges in the 5–75 K (V) and 10–50 K (Fe) range, respectively. Palette colors highlight the temperatures corresponding to the magnetic transition region. In the middle, the $k\chi(k)$ spectra measured at 10 K (blue dots) and the best fits (black line) are shown for V and Fe K edges. The neighbor shell contributions used in the data refinement (VN_n and FeN_n) are shown for completeness, vertically shifted for clarity. Bottom black curves are the experimental minus best-fit residues: $k\chi^{\text{exp}} - k\chi^{\text{fit}}$.

refinement allows us to shed light on the weak structural modification associated with the magnetic transitions.

The EXAFS data analysis involved fitting the $k\chi(k)$ experimental spectra in the 3–14.5 and 3–16 \AA^{-1} range for V and Fe K edges, respectively. The theoretical curves were calculated using the standard EXAFS formula [34], considering the structural contribution from main neighbor coordination shells and selected multiple scattering (MS) terms, to reproduce the average local atomic structure around the absorber up to approximately 4 \AA (Fig. 7). To select the relevant contributions suitable for the EXAFS data refinement, and to calculate the photoelectron scattering amplitude and phase functions using the FEFF8 program [35], the Fe local structure has been modeled on the basis of FeVO_4 crystallographic phase combining literature [36] and our XRD pattern analysis.

The EXAFS analysis is unable to distinguish between the three different V(1-3) or Fe(1-3) sites within the structure. Therefore, we considered an average structure surrounding the generic absorber. The average crystallographic structure around V comprises four oxygen bonds around $\bar{R}^c(\text{VO}_1) \simeq 1.8 \text{ \AA}$. A second oxygen shell is expected at around $\bar{R}^c(\text{VO}_2) \simeq 2.9 \text{ \AA}$ for the V(2) site. The V-Fe shell is broadly distributed between 3.1 and 3.7 \AA . The model curve was built with two VO_1 and VO_2 shells with multiplicities 4 and 1.33, respectively. A single shell has been considered for the VFe shell around 3.4 \AA and the analysis reveals that signals from MS paths of certain V-O-Fe configurations with relatively large angles are also significant, in particular from double (around 3.6 \AA) and triple (around 3.9 \AA) scattering paths, labeled as VOFe and VOFeO in the following. The single and MS contributions produce antiphase signals (Fig. 7) that give rise to strong correlation effects, especially between their multiplicities, which are affected by large absolute uncertainties. After a trial and error procedure, we fixed the V-Fe multiplicity to 4 and those of VOFe and VOFeO paths to 2

and 1, respectively. The multiplicity numbers, the energy shift (ΔE , accounting for the difference between the edge energy used in the EXAFS extraction and that used for calculating the amplitude and phase shift functions), and the S_o^2 (accounting for inelastic losses) were kept fixed and equal for the refinement of all the temperature-dependent EXAFS spectra leaving 10 free parameters for the 5 shells used in the model. Attempts to include other contributions make the refinement unstable and poorly reliable due to their overlap and the high correlations among the fitting parameters.

The average crystallographic structure around Fe ions consists of 5.67 oxygen neighbors (six from the FeO_6 and five from the FeO_5 polyhedra) at the average distance $\bar{R}^c(\text{FeO}_1) \simeq 1.98 \text{ \AA}$. There are then on average 5/3 Fe atoms [one around the Fe(1) and two from each Fe(2) and Fe(3) sites] around $\bar{R}^c(\text{FeFe}) \simeq 3.06 \text{ \AA}$ and approximately 5.6 vanadium atoms at $\bar{R}^c(\text{FeV}) \simeq 3.4 \text{ \AA}$ broadly distributed between 3.2 and 3.6 \AA . The analysis demonstrates a significant contribution only from the double scattering contribution from Fe-O-V configurations, which has been considered with 2/3 multiplicity.

The ΔE and the S_o^2 parameters were kept fixed. The Fe-O average coordination number was fixed to 5.67, but after preliminary tests, the analysis required the Fe-O distribution to be split into two subshells $\text{FeO}_{1a,b}$ with $N(\text{FeO}_{1a}) : N(\text{FeO}_{1b}) = 5 : 1$, respectively, found around $R_{O_1a} \simeq 1.98 \text{ \AA}$ and $R_{O_1b} \simeq 2.31 \text{ \AA}$, in agreement with crystallographic data. The multiplicity of the Fe-Fe shell is kept fixed at 1.67, and the $R(\text{FeFe})$ distance is found around 3.08 \AA in agreement with the average crystallographic distance. The Fe-V distance is found around $R(\text{FeV}) \simeq 3.43 \text{ \AA}$, which is in good agreement with the average crystallographic value and in agreement with the V K -edge EXAFS analysis. In preliminary tests, the FeV multiplicity number was $\simeq 2$, systematically lower than expected from the crystallographic model but in agreement with the value of 3 ± 5 reported in the literature [32]. Such a low value should be mainly ascribed to the evident antiphase effect between FeFe, FeV, and FeOV signals (Fig. 7) that hides them from each other. In the analysis, we kept the Fe-V multiplicity fixed at 2 for all the temperatures. The best fit also requires including the multiple scattering terms from Fe-O-V configurations, enhanced by its relatively large forward scattering. The refined half path length $R_{\text{FeOV}} = 3.62 \text{ \AA}$ is in good agreement with the crystallographic length expected at 3.63 \AA . This schema allows a satisfactory best-fit fitting of the experimental data using five contributions (shells) and ten free parameters (we used the F-test to check the statistical significance [37]). Attempts to include other contributions make the refinement unstable and poorly reliable due to their overlap and the high correlations among the fitting parameters.

Examples of the best fit for V and Fe spectra are presented in Fig. 7. The values of the structural parameters averaged over the whole temperature ranges (\bar{R} and $\bar{\sigma}^2$) for the five shells used in the analysis are shown in Table I. To present the evolution of the structural parameters as a function of the temperature and highlight the relationship with the transition temperatures, we present in Fig. 8 their relative variations as $\Delta R/\bar{R} = (R(T) - \bar{R})/\bar{R}$ and $\Delta\sigma^2/\bar{\sigma}^2 = (\sigma^2(T) - \bar{\sigma}^2)/\bar{\sigma}^2$. Looking at the data in Fig. 8, it is clear that when crossing the

TABLE I. Mean of the values of the structural parameters of each coordination shell averaged over the whole temperature range analyzed. The range of variation (maximum-minimum) of each parameter is given in square brackets. Multiplicity numbers were kept fixed.

Shell	N^*	\bar{R} (Å)	$\overline{\sigma^2} \times 10^2$ (Å ²)
V <i>K</i> edge			
VO ₁	4	1.7208 [0.0007]	0.577 [0.037]
VO ₂	1.33	2.7467 [0.0038]	0.67 [0.18]
VFe	4	3.4410 [0.0041]	0.578 [0.088]
VOFe	2	3.5706 [0.0046]	0.93 [0.18]
VOFeO	1	3.9968 [0.0099]	2.72 [0.38]
Fe <i>K</i> edge			
FeO _{1a}	4.72	1.9825 [0.0010]	0.472 [0.031]
FeO _{1b}	0.94	2.3063 [0.0041]	1.10 [0.22]
FeFe	1.67	3.0848 [0.0065]	0.364 [0.051]
FeV	2	3.4299 [0.0068]	0.48 [0.11]
FeOV	0.66	3.650 [0.010]	0.25 [0.12]

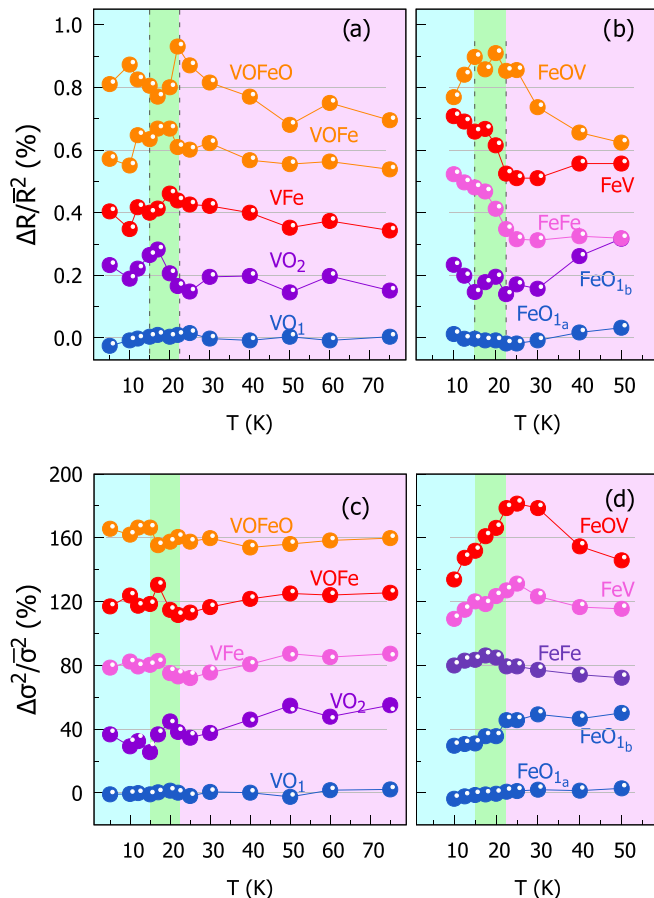


FIG. 8. Structural parameters obtained refining the V [left panels (a),(c)] and Fe [right panels (b),(d)] EXAFS data. To facilitate comparison of the data in the different shells, the relative variations of the parameters are shown: \bar{X} being the average value of the parameter ($X = R, \sigma^2$) over the measured temperature range, and $\Delta X = X(T) - \bar{X}$ is the difference with respect to the average value as a function of T . Data are vertically shifted for the sake of clarity; gray lines represent the \bar{X} values, vertically shifted for clarity. Transition temperatures are highlighted by color regions.

magnetic transition temperatures, there is a greater effect for next-neighbor distances, while the closer shells depict very tiny effects, with the VO₁ and FeO_{1a} distances changing less than 0.1% and their MSRD changing much less than 5% in the whole temperature range.

IV. DISCUSSIONS AND RESULTS

A. Specificity of XAFS probes

Before discussing the results, it is worth recalling some of the peculiarities of the techniques used, in particular XAFS and XRD, which allow us to appreciate the complementary aspects of the information obtained. The XRD signal originates from structural features that repeat periodically in the unit cells, while features without translational symmetry contribute only to a diffuse background halo. In contrast, the XAFS signal originates from the local structure surrounding the absorber, regardless of whether it exhibits short- or long-range order. Several examples illustrate such a difference between XAFS and XRD information (see Ref. [38] for a recent representative one), but a very a classic example illustrating the difference between crystallographic and short-range order is found in pseudobinary semiconductor alloys $(A_{1-x}B_x)C$ in which [39] XRD demonstrates the lattice parameters and distances between crystallographic sites changing linearly as a function of x , strictly following Vegard's law, while the EXAFS analysis demonstrates that the interatomic distances A-C and B-C remain very similar to those found in the end compounds due to the rigidity of the covalent bonds. This apparent discrepancy is due to the random substitution of A by B on the lattice, which results in a lack of translation symmetry (long-range order), which is why the diffractograms show no splitting or broadening of the diffraction peaks. In general, nonperiodic features in the distribution of atoms mean that the interatomic distances obtained from EXAFS analysis can also be very different from the distances between atomic sites in the periodic lattice. To discriminate between short-range order and crystallographic lattice, we will refer to XRD results as the *distances between the crystallographic sites*.

In addition to information about interatomic distances, the XAFS signal contains further details about the atomic structure and electrical nature of the absorber. Traditionally the XAFS signal is divided into EXAFS (extended) and XANES (near-edge) regions. In the EXAFS region, the signal is dominated by single (SS) photoelectron scattering processes and selected multiple scattering (MS) phenomena from almost collinear atomic configurations, which are enhanced by the forward scattering effect [40,41].

The EXAFS signal is generally modeled using the standard EXAFS formula describing the average local structure around the absorber as a sum of Gaussian-shaped interatomic shells, each one defined giving its multiplicity (N), average distance (R), and mean square relative displacement (MSRD, σ^2) [41]. The same model applies to MS terms in which R corresponds to half the photoelectron scattering path length. The σ^2 includes a temperature-dependent contribution, accounting for thermally activated lattice vibrations, plus a temperature-independent static contribution: $\sigma^2 = \sigma_E^2(T) + \sigma_{\text{static}}^2$.

The temperature-dependent contribution is well reproduced by a correlated Einstein model [42]

$$\sigma_E^2(T) = \frac{\hbar}{\mu\omega_E} \coth\left(\frac{\hbar\omega_E}{2k_B T}\right).$$

Notice that at low temperatures (T less than about 60–70 K), $\sigma_E^2(T)$ is generally roughly constant [41,42]. Systematic effects, including those associated with the theoretical calculation of the amplitude and phase functions, and the correlation between the best-fit parameters, make the absolute accuracy of the structural parameters obtained from the EXAFS fitting relatively low compared to the accuracy of XRD, so an accuracy of around 0.1–0.05 % for interatomic distances and around 5% for MSRDS is normally accepted.

However, by relying on the stability and reproducibility of the experimental setup and by reducing the correlations between the fitting parameters (e.g., by fixing ΔE and coordination numbers), it is possible to increase by more than an order of magnitude the accuracy with which the relative variations in structural parameters in a sample can be determined as a function of external parameters such as temperature, as shown by studies about thermal expansion of solids [42]. When analyzing the next-neighbor shells, the accuracy decreases due to the superposition of different signals, the correlation between the parameters, and the need to merge certain contributions and/or neglect others. However, the relative variations of the parameters allow even tiny structural effects to come to the fore.

The XANES region is rich in both structural and electronic information [43], and, due to the Debye-Waller factor $e^{-2k^2\sigma^2}$ in the XAFS model, the XANES signal is generally weakly dependent on temperature. The edge position is specific to the photoabsorber valence state. Given the extended mean free path of low-energy photoelectrons, multiple scattering effects become significant at various orders (full multiple scattering region) making the XANES features highly sensitive to the coordination symmetry around the photoabsorber. Also, the preedge analysis often yields valuable insights, especially when examining the K -edges of $3d$ metals like Fe and V in our case. In fact, the features observed in the preedge of these $3d$ metals arise from dipole-forbidden transitions to localized d -states of Fe and V. The mixing of the metal d -states with the ligands' p -states may enhance the resonance by increasing the dipole-allowed transition probability [44,45]. For example, the p - d hybridization is minimal for regular FeO_6 octahedra, while it increases by removing the octahedral symmetry, such as reducing the average coordination and/or distorting the octahedra, and it becomes maximal, for example, in VO_4 tetrahedra [45]. Given these facts, the energy position (centroid) and area of the preedge peak are widely accepted to accurately assess the average Fe valence state, coordination number, and coordination geometry in a sample [44–47]. With these considerations in mind, we proceed to discuss the obtained results.

B. Experimental results

The V and Fe K -edge XANES behaves equally as a function of temperature (the standard deviation between the normalized spectra being less than 10^{-3}), preventing us from

appreciating qualitatively any difference. The PCA reveals modification in the trend of w_1 and w_2 weight as a function of T (Fig. 6), correlated with the magnetic transition temperatures. The intense preedge peak A in the V preedge with an area of 2.58 eV is located at 5469.69 eV and remains stable within ± 0.05 eV (area) and ± 0.05 eV (shift) over the whole temperature range. The raising of the edge is consistent with the V^{5+} valence state. The Fe- K preedge features exhibit two distinct peaks, labeled A and B in Fig. 6. Peak B is attributed to dipole-allowed photoelectron transitions to s and p Fe empty states [48]. Peak A corresponds to transitions to the p - d hybridized states; the centroid at 7112.8 eV is consistent with Fe^{3+} valence, and the area (0.12 eV) is consistent with distorted FeO_{6-x} coordination, which corresponds to the average Fe local coordination in the FeVO_4 crystallographic structure. For both V and Fe, the preedge fitting does not exhibit demonstrable changes correlated to the magnetic transition, remaining within the bounds of uncertainty. This finding demonstrates that the average valence of V and Fe atoms and that the Fe/V polyhedra show minimal influence from the magnetic transitions.

Further details regarding the average local structure around V and Fe atoms are obtained analyzing the EXAFS region. The quantitative analysis (Table I and Fig. 8) shows the V-O nearest-neighbor shell without appreciable changes as a function of temperature in between $R(\text{VO}) \simeq 1.7208 \pm 0.007$ Å. Larger effects become evident looking at the next-neighbor shells, in particular the V-O₂ shell and the MS contributions involving V-O-Fe configurations. Much more striking effects can be observed when looking at the structure around Fe, with the magnetic active ion being in the FeVO_4 structure.

The Fe K -edge EXAFS analysis reveals a bimodal Fe-O nearest-neighbor distribution with 4.7 O_{1a} neighbors at about 1.983 Å and 0.9 O_{1b} atoms at about 2.31 Å (Table I). The average Fe-O_{1a} distances and MSRD remain unchanged within less 0.1% and less than 5% across the magnetic transition and the whole temperature range investigated (Fig. 8). The Fe-O_{1b} shell exhibits slight changes upon cooling through the transition temperatures with a marginal decrease in the distance ($< 0.2\%$) and an approximate 10% reduction in MSRD. Notably, the O_{1b} contribution constitutes merely 1/6 of the average Fe-O₁ coordination. This, together with the small size of the effect, explains why it produces a negligible effect in the XANES (preedge) region.

More interesting is what happens looking at the next-neighbor shells in which microstructural effects linked with the magnetic transitions become much more evident (Fig. 8). Specifically, the Fe-Fe, Fe-V, and Fe-O-V distances exhibit a sudden increase of more than 0.2% during the cooling across the transitions, and the MSRD contributions depict clear maxima just close to T_{N1} in a region in which σ^2 is expected to be constant due to the freezing of the thermally activated lattice vibrations. Considering the very unchanged Fe/V-O nearest-neighbor distances, this trend in the next-nearest neighbors is likely associated with changes in the tilting of the FeO_n and VO_4 polyhedra, which serves as a hallmark of alterations in super-exchange (SE) and super-super-exchange (SSE) interaction pathways involving Fe^{3+} -O-V⁵⁺-O- Fe^{3+} , across these transitions.

The analysis of the Raman spectra supports the conclusions drawn from the XAFS findings. A detailed discussion on the room-temperature Raman spectroscopy of the FeVO_4 compound can be found elsewhere [16]. When examining the temperature-dependent Raman spectra, the absence of notable variations in the number of phonon modes and the overall similar spectral shape within the measured temperature range indicates that the magnetic transitions in FeVO_4 do not align with any structural phase transitions. We have observed drastic deviations in the anharmonic phonon behavior for some of the phonon modes corresponding to the bridging of V-O...Fe stretching and a mixture of bending modes of Fe-O and V-O bonds at relatively high temperatures (around 70 K) compared to the transition temperatures (15.65 and 21.85 K). This significant deviation can be attributed to the presence of short-range magnetic ordering in this system, as reported in NMR studies of FeVO_4 [12]. The emergence of short-range magnetic order cooling below 70 K is consistent with the trend in the structural parameters corresponding to the Fe-O-V configuration (Fig. 8) revealed by EXAFS analysis, which anticipates the magnetic transition temperature, and suggests that the onset of spin-phonon coupling is active well above the T_{N1} temperatures. The temperature trend of the modes corresponding to V-O and Fe-O bond stretching and bending (at 970 and 914 cm^{-1} and at 343 and 106 cm^{-1} , respectively) shows only minor changes crossing the magnetic transition temperatures (Fig. 5). This finding is consistent with the EXAFS results pointing out that minimal structural changes of V/Fe- O_n coordination polyhedra are associated with magnetic transitions. On the contrary, we have identified certain phonon modes associated with V-O...Fe stretching and a mixture of bending modes of Fe and V bonds (at 774, 632, 320, and 316 cm^{-1}) that exhibit abrupt frequency changes at both the magnetic transition temperatures (T_{N1} and T_{N2}) (Fig. 5). This trend, again in agreement with EXAFS results, likely represents the structural counterpart of changes in spin-lattice/phonon coupling across the transitions [49,50]. At T_{N2} , the next-nearest-neighbor interactions along the Fe-O-V-O-Fe pathways are the dominant factor that causes the spiral magnetic ordering and onset-induced ferroelectric ordering in FeVO_4 . This type of phonon softening has also been observed in very well-known multiferroic materials with the AMnO_3 ($A = \text{Tb, Dy}$) structure [51]. Importantly, the softening of these phonon frequencies in our study is associated with the dilation of the unit cell as the temperature increases, as demonstrated in our previous studies [9].

The SR-XRD data analysis shows the crystallographic changes that occur across the magnetic transition temperatures, the major effects being activated cooling below T_{N2} . In particular, the largest effect is found on the FeO_5 polyhedra [Fe(2) site], while the FeO_6 polyhedra [Fe(1) and Fe(3) sites] show smaller changes. In particular, $\bar{d}(\text{Fe}(3)\text{O}_6)$ slightly decreases ($\approx 1\%$), while $\bar{d}(\text{Fe}(2)\text{O}_5)$ increases by about 1.2% crossing T_{N2} . The polyhedral distortion Δ_d shows no significant changes for the FeO_6 sites but increases smoothly up to about 10% for the $\text{Fe}(2)\text{O}_5$ site. The changes in Fe-Fe and Fe-V distances have been calculated as a function of temperature to demonstrate the tilting of the polyhedra during the magnetic transition. These calculations suggest variations in the Fe-O-Fe and Fe-O-V angles, respectively.

Below the transition, the Fe-Fe distances change by approximately 0.15%, while the Fe-V distances corresponding to the three distinct Fe- O_n polyhedra surrounding the VO_4 groups change by approximately 0.3% across the transitions. These observations align with the results obtained from EXAFS analysis, indicating the significant role of polyhedral tilting in magnetic transitions. Specifically, the relative tilting of $\text{FeO}_n\text{-VO}_4$ polyhedra is associated with the superexchange (SSE) interaction pathway ($\text{Fe}^{3+}\text{-O-V}^{5+}\text{-O-Fe}^{3+}$) across the transitions.

V. CONCLUSIONS

We have investigated the local structural modification across the magnetic and multiferroic transitions in the FeVO_4 compound combining temperature-dependent complementary probes, namely SR-XRD, Raman, and EXAFS measurements. The Rietveld refinement of temperature-dependent XRD patterns as a function of temperature reveals the unit cell changes associated with the magnetic transition. Raman and XAFS analysis, probing the short-range structure, provides further details. The analysis of temperature-dependent (5–300 K) Raman spectra depicts evident changes related to the transitions that can be interpreted as the signatures of spin-lattice/phonon coupling across the transitions due to the polar displacements at T_{N2} developing electrical polarization in FeVO_4 . The analysis of the V- and Fe- K edge XAFS spectra in the XANES and EXAFS regions demonstrates the very unchanged preedge features in V/Fe K -edge XANES as a function of temperature, which excludes major changes in V/Fe valence state or average VO_4 or FeO_n polyhedra distortions related to the transitions at $T_{N1,2}$. The very constant V/Fe-O bond lengths across the transitions are further confirmed by the analysis of the EXAFS spectra. On the contrary, the EXAFS data analysis clearly shows an evolution of the V/Fe next-neighbor coordination shells associated with the magnetic transitions, with changes in the V/Fe-Fe distances and Fe-O-V path geometry tuning the temperature across $T_{N1,2}$, likely representing the microstructural counterpart of the changes in the SSE interactions along the $\text{Fe}^{3+}\text{-O-V}^{5+}\text{-O-Fe}^{3+}$ pathway.

The macroscopic magnetic response of these complex materials, such as FeVO_4 , depends critically on the local coordination geometry and atomic interactions. This study demonstrates that experimental methods that can provide complementary insight into the atomic-scale structural changes associated with magnetic transitions are essential for a reliable understanding of the atomic-scale mechanisms involved in the changes in physical properties.

ACKNOWLEDGMENTS

G.B. thanks the University Grants Commission (UGC), New Delhi for Dr. D. S. Kothari Post-Doctoral Fellowship Award (2021) (Grant No. F.4-2/2006 (BSR)/PH/20-21/0166). Financial support by the Department of Science and Technology, India provided within the framework of India @ DESY collaboration for measurements at PETRA-III, Germany is acknowledged. M.L.R. thanks CONIUCET (AR) for his doctoral fellowship. C.M. acknowledges the MUR (IT) support (Grant: Dipartimenti di Eccellenza 2023–2027, Art. 1, 314–337 Legge 232/2016).

- [1] N. A. Spaldin and R. Ramesh, Advances in magnetoelectric multiferroics, *Nat. Mater.* **18**, 203 (2019).
- [2] D. Khomskii, Classifying multiferroics: Mechanisms and effects, *Physics* **2**, 20 (2009).
- [3] Y. Tokura, S. Seki, and N. Nagaosa, Multiferroics of spin origin, *Rep. Prog. Phys.* **77**, 076501 (2014).
- [4] M. Gajek, M. Bibes, S. Fusil, K. Bouzehouane, J. Fontcuberta, A. Barthelemy, and A. Fert, Tunnel junctions with multiferroic barriers, *Nat. Mater.* **6**, 296 (2007).
- [5] A. Dixit, G. Lawes, and A. B. Harris, Magnetic structure and magnetoelectric coupling in bulk and thin film FeVO_4 , *Phys. Rev. B* **82**, 024430 (2010).
- [6] A. Dixit, P. Chen, G. Lawes, and J. Musfeldt, Electronic structure and polaronic excitation in FeVO_4 , *Appl. Phys. Lett.* **99**, 141908 (2011).
- [7] A. Young and C. Schwartz, High pressure forms of CrVO_4 and FeVO_4 , *Acta Crystallogr.* **15**, 1305 (1962).
- [8] S. Lopez-Moreno, D. Errandonea, J. Pellicer-Porres, D. Martinez-Garcia, S. J. Patwe, S. N. Achary, A. K. Tyagi, P. Rodriguez-Hernandez, A. Munoz, and C. Popescu, Stability of fevo4 under pressure: An x-ray diffraction and first-principles study, *Inorg. Chem.* **57**, 7860 (2018).
- [9] G. Bera, A. Surampalli, A. Mishra, P. Mal, V. R. Reddy, A. Banerjee, A. Sagdeo, P. Das, and G. R. Turpu, Magnetolattice coupling, magnetic frustration, and magnetoelectric effect in the Cr-doped FeVO_4 multiferroic material and their correlation with structural phase transitions, *Phys. Rev. B* **100**, 014436 (2019).
- [10] A. Daoud-Aladine, B. Kundys, C. Martin, P. G. Radaelli, P. J. Brown, C. Simon, and L. C. Chapon, Multiferroicity and spiral magnetism in FeVO_4 with quenched fe orbital moments, *Phys. Rev. B* **80**, 220402(R) (2009).
- [11] A. Dixit and G. Lawes, Development of electrical polarization at an antiferromagnetic transition in FeVO_4 , *J. Phys.: Condens. Matter* **21**, 456003 (2009).
- [12] J. Zhang, L. Ma, J. Dai, Y. P. Zhang, Z. He, B. Normand, and W. Yu, Spin fluctuations and frustrated magnetism in multiferroic FeVO_4 , *Phys. Rev. B* **89**, 174412 (2014).
- [13] B. Kundys, C. Martin, and C. Simon, Magnetoelectric coupling in polycrystalline FeVO_4 , *Phys. Rev. B* **80**, 172103 (2009).
- [14] L. Zhao, M. P. Wu, K.-W. Yeh, and M.-K. Wu, Multiferroic studies on polycrystalline FeVO_4 , *Solid State Commun.* **151**, 1728 (2011).
- [15] A. Kumarasiri, E. Abdelhamid, A. Dixit, and G. Lawes, Effect of transition metal doping on multiferroic ordering in FeVO_4 , *Phys. Rev. B* **91**, 014420 (2015).
- [16] G. Bera, V. Reddy, P. Rambabu, P. Mal, P. Das, N. Mohapatra, G. Padmaja, and G. Turpu, Triclinic–monoclinic–orthorhombic (T–M–O) structural transitions in phase diagram of $\text{FeVO}_4\text{-CrVO}_4$ solid solutions, *J. Appl. Phys.* **122**, 115101 (2017).
- [17] http://www.rrcat.gov.in/technology/accel/srnl/beamlines/mcd_pes.html.
- [18] A. P. Hammersley, FIT2D: A multi-purpose data reduction, analysis and visualization program, *J. Appl. Cryst.* **49**, 646 (2016).
- [19] J. Rodríguez-Carvajal, Recent advances in magnetic structure determination by neutron powder diffraction, *Phys. B: Condens. Matter* **192**, 55 (1993).
- [20] K. Momma and F. Izumi, VESTA 3 for three-dimensional visualization of crystal, volumetric and morphology data, *J. Appl. Crystallogr.* **44**, 1272 (2011).
- [21] E. Welter, R. Chernikov, M. Herrmann, and R. Nemausat, A beamline for bulk sample x-ray absorption spectroscopy at the high brilliance storage ring petra III, *AIP Conference Proceedings No. 2054* (AIP, New York, 2019), p. 040002.
- [22] C. R. Harris, K. J. Millman, S. J. van der Walt, R. Gommers, P. Virtanen, D. Cournapeau, E. Wieser, J. Taylor, S. Berg, N. J. Smith, R. Kern, M. Picus, S. Hoyer, M. H. van Kerkwijk, M. Brett, A. Haldane, J. F. del R'io, M. Wiebe, P. Peterson, P. G'erard-Marchant *et al.*, Array programming with NumPy, *Nature (London)* **585**, 357 (2020).
- [23] C. Meneghini, F. Bardelli, and S. Mobilio, Estra-fitexa: A software package for exafs data analysis, *Nucl. Instrum. Methods Phys. Res., Sect. B* **285**, 153 (2012).
- [24] See Supplemental Material at <http://link.aps.org/supplemental/10.1103/PhysRevB.109.075138> for further details. Figures S1–S4 and Tables SI–SIII provide XRD data analysis details and crystal structural information. The data shown in Figs. S5,S6 go into the details of Raman analysis, and the plots in Fig. S7 show the Fourier transform of EXAFS data and best fit.
- [25] I. Jolliffe, *Principal Component Analysis* (Springer Verlag, New York, 2002).
- [26] J. Demšar, T. Curk, A. Erjavec, Črt Gorup, T. Hočevar, M. Milutinovič, M. Možina, M. Polajnar, M. Toplak, A. Starič, M. Štajdohar, L. Umek, L. Žagar, J. Žbontar, M. Žitnik, and B. Zupan, Orange: Data mining toolbox in python, *J. Mach. Learn. Res.* **14**, 2349 (2013).
- [27] X. Shen, S. Ye, L. Xu, R. Hu, L. Jin, H. Xu, J. Liu, and W. Liu, Study on baseline correction methods for the fourier transform infrared spectra with different signal-to-noise ratios, *Appl. Opt.* **57**, 5794 (2018).
- [28] M. Balkanski, R. F. Wallis, and E. Haro, Anharmonic effects in light scattering due to optical phonons in silicon, *Phys. Rev. B* **28**, 1928 (1983).
- [29] V. Brázdová, M. V. Ganduglia-Pirovano, and J. Sauer, Crystal structure and vibrational spectra of ALVO_4 a DFT study, *J. Phys. Chem. B* **109**, 394 (2005).
- [30] D. C. Koningsberger and R. Prins, X-ray absorption: principles, applications, techniques of EXAFS, SEXAFS, and XANES (John Wiley & Sons, New York, 1988).
- [31] E. J. O'Loughlin, M. I. Boyanov, and K. M. Kemner, Reduction of Vanadium(V) by Iron(II)-bearing minerals, *Minerals* **11**, 316 (2021).
- [32] F. Liu, H. He, Z. Lian, W. Shan, L. Xie, K. Asakura, W. Yang, and H. Deng, Highly dispersed iron vanadate catalyst supported on TiO_2 for the selective catalytic reduction of NO_x with NH_3 , *J. Catal.* **307**, 340 (2013).
- [33] G. Bera, A. Surampalli, P. Mal, V. Reddy, K. Kumar, A. Sagdeo, P. Rajput, P. Das, and G. Turpu, Structural, magnetic, dielectric and ^{57}Fe mössbauer spectroscopic studies on $\text{Fe}_{1-x}\text{Ce}_x\text{VO}_4$: A type-II multiferroic material, *J. Mater. Sci.: Mater. Electron.* **32**, 7399 (2021).
- [34] J. Rehr and R. C. Albers, Theoretical approaches to x-ray absorption fine structure, *Rev. Mod. Phys.* **72**, 621 (2000).
- [35] A. L. Ankudinov, B. Ravel, J. J. Rehr, and S. D. Conradson, Real-space multiple-scattering calculation and interpretation of x-ray-absorption near-edge structure, *Phys. Rev. B* **58**, 7565 (1998).

- [36] B. Robertson and E. Kostiner, Crystal structure and mössbauer effect investigation of FeVO_4 , *J. Solid State Chem.* **4**, 29 (1972).
- [37] A. Michalowicz, K. Provost, S. Laruelle, A. Mimouni, and G. Vlaic, F-test in EXAFS fitting of structural models, *J. Synch. Radiat.* **6**, 233 (1999).
- [38] G. Schuck, D. M. Töbrens, D. Wallacher, N. Grimm, T. S. Tien, and S. Schorr, Temperature-dependent EXAFS measurements of the Pb L3-edge allow quantification of the anharmonicity of the Lead–Halide bond of Chlorine-Substituted Methylammonium (MA) Lead Triiodide, *J. Phys. Chem. C* **126**, 5388 (2022).
- [39] J. B. Boyce and J. C. Mikkelsen, Jr., Local structure of pseudobinary semiconductor alloys: An x-ray absorption fine structure study, *J. Cryst. Growth* **98**, 37 (1989).
- [40] A. Filipponi, A. Di Cicco, and C. R. Natoli, X-ray-absorption spectroscopy and n-body distribution functions in condensed matter. I. Theory, *Phys. Rev. B* **52**, 15122 (1995).
- [41] G. Bunker, Theory, in *Introduction to XAFS* (Cambridge University Press, Cambridge, UK, 2010), pp. 106–133.
- [42] M. Vaccari and P. Fornasini, Einstein and Debye models for EXAFS parallel and perpendicular mean-square relative displacements, *J. Synch. Radiat.* **13**, 321 (2006).
- [43] M. Benfatto and C. Meneghini, A close look into the low energy region of the xas spectra: The xanes region, in *Synchrotron Radiation: Basics, Methods and Applications*, edited by S. Mobilio, F. Boscherini, and C. Meneghini (Springer, Berlin, 2015), pp. 213–240.
- [44] T. E. Westre, P. Kennepohl, J. G. DeWitt, B. Hedman, K. O. Hodgson, and E. I. Solomon, A multiplet analysis of Fe K-edge $1s \rightarrow 3d$ Pre-Edge features of iron complexes, *J. Am. Chem. Soc.* **119**, 6297 (1997).
- [45] M. Wilke, F. Farges, P.-E. Petit, G. E. Brown, and F. Martin, Oxidation state and coordination of Fe in minerals: An Fe K-XANES spectroscopic study, *Am. Mineral.* **86**, 714 (2001).
- [46] G. Giuli, S. G. Eeckhout, E. Paris, C. Koeberl, and G. Pratesi, Iron oxidation state in impact glass from the K/T boundary at Beloc, Haiti, by high-resolution XANES spectroscopy, *Meteorit. Planet. Sci.* **40**, 1575 (2005).
- [47] G. Giuli, M. R. Cicconi, S. G. Eeckhout, G. Pratesi, E. Paris, and L. Folco, Australasian microtektites from antarctica: XAS determination of the Fe oxidation state, *Meteorit. Planet. Sci.* **49**, 696 (2014).
- [48] W. Phoohinkong, K. Boonyarattanakalin, W. Mekprasart, S. Pavasupree, and W. Pecharapa, Nonlocal XANES pre-edge feature of FeTiO_3 ilmenite-type at Ti and Fe K-edge, *Radiat. Phys. Chem.* **174**, 108919 (2020).
- [49] C. Toulouse, C. Martin, M.-A. Measson, Y. Gallais, A. Sacuto, and M. Cazayous, Magnetic transitions in $\text{CaMn}_7\text{O}_{12}$: Raman observation of spin-phonon couplings, *Phys. Rev. B* **99**, 024303 (2019).
- [50] A. Panchwanee, V. R. Reddy, A. Gupta, and V. Sathe, Study of spin-phonon coupling and magnetic field induced spin reorientation in polycrystalline multiferroic GdFeO_3 , *Mater. Chem. Phys.* **196**, 205 (2017).
- [51] P. J. Graham, P. Rovillain, M. Bartkowiak, E. Pomjakushina, K. Conder, M. Kenzelmann, and C. Ulrich, Spin-phonon and magnetoelectric coupling in oxygen-isotope substituted TbMnO_3 investigated by raman scattering, *Phys. Rev. B* **105**, 174438 (2022).